

Magnetic structure of the $S=1$ $\text{Ni}_5(\text{TeO}_3)_4\text{Br}_2$ layered system governed by magnetic anisotropy

M. Pregelj,¹ A. Zorko,¹ H. Berger,² H. van Tol,³ L. C. Brunel,³ A. Ozarowski,³ S. Nellutla,³ Z. Jagličič,⁴ O. Zaharko,^{5,*} P. Tregenna-Piggott,⁵ and D. Arčon^{1,6,†}

¹*Institute Jozef Stefan, Jamova 39, 1000 Ljubljana, Slovenia*

²*Institute of Physics of Complex Matter, EPFL, 1015 Lausanne, Switzerland*

³*High Magnetic Field Laboratory, Tallahassee, Florida 32310, USA*

⁴*Institute of Mathematics, Physics and Mechanics, 1000 Ljubljana, Slovenia*

⁵*Laboratory for Neutron Scattering, ETHZ and Paul Scherrer Institute, CH-5232 Villigen, Switzerland*

⁶*Faculty of Mathematics and Physics, University of Ljubljana, Jadranska 19, 1000 Ljubljana, Slovenia*

(Received 8 June 2007; revised manuscript received 16 August 2007; published 4 October 2007)

Magnetization, neutron diffraction, and antiferromagnetic resonance measurements were employed to investigate the magnetic ground state of $\text{Ni}_5(\text{TeO}_3)_4\text{Br}_2$ single crystal. Despite the layered topology of the Ni^{2+} sites, typical for frustrated antiferromagnets, the system orders antiferromagnetically below $T_N=29$ K. Noncollinear arrangements of the Ni sublattices having a very complex temperature dependence were found from the neutron diffraction and magnetization measurements. Single-ion anisotropy, associated with the strongly distorted Ni-centered octahedra, has the same magnitude as the antiferromagnetic exchange interaction. The effect of these anisotropies prevails over the geometrical frustration leading to a long-range magnetic ordering below T_N .

DOI: 10.1103/PhysRevB.76.144408

PACS number(s): 75.50.Ee, 76.50.+g

I. INTRODUCTION

Antiferromagnets with spins sitting on the vertices of triangular arrays are prototypes of geometrically frustrated systems.¹ In these systems, the antiferromagnetic interactions cannot all be simultaneously satisfied. Such frustration results in a highly degenerate competing ground states, enhances quantum fluctuations, and precludes the occurrence of a long-range Néel order. The presence of magnetic anisotropies can, on the other hand, act against frustration by lifting the degeneracy, opening a gap in the excitation spectrum, suppressing quantum fluctuations, and stabilizing a long-range magnetically ordered state. In real systems, it is the competition between the magnetic frustration and the magnetic anisotropy that defines their ground states.

Search for novel two-dimensional magnetic systems recently leads to the investigation of the ternary phase diagram $\text{NiO-NiCl}_2\text{-TeO}_2$ and to the synthesis of new transition-metal tellurium oxychlorides with the general chemical formula $\text{Ni}_5(\text{TeO}_3)_4\text{X}_2$ ($\text{X}=\text{Br}, \text{Cl}, \text{I}$).² Their structure has the space group $C2/c$ with the room temperature unit cell parameters $a=20.715$ Å, $b=5.296$ Å, $c=16.408$ Å, and $\beta=124.8^\circ$ (parameters are listed for $\text{X}=\text{Br}$). The unit cell contains three crystallographically inequivalent Ni^{2+} sites, called Ni1, Ni2, and Ni3 (Fig. 1) arranged in some kind of a “claw” $[\text{Ni}_5\text{O}_{17}\text{X}_2]$ basic unit made of two connected triangles with Ni1 in the center. Finally, $[\text{Ni}_5\text{O}_{17}\text{X}_2]$ units form a layered structure via corner sharing (Fig. 1).

The triangular based Ni^{2+} topology in $\text{Ni}_5(\text{TeO}_3)_4\text{X}_2$ has thus all characteristics of frustrated systems. On the other hand, all Ni^{2+} sites have strongly distorted octahedral environments and thus a significant magnetic anisotropy is expected. In this work, we try to resolve the question which of the two properties prevails and determines the ground state in $\text{Ni}_5(\text{TeO}_3)_4\text{Br}_2$.

A high-temperature Curie-Weiss dependence of the magnetic susceptibility² suggested antiferromagnetic interactions

between Ni^{2+} (electronic configuration $3d^8$) $S=1$ spins. The preliminary magnetic susceptibility data² also found a small anomaly at low temperatures indicating a magnetic transition at around $T_N=29$ K for $\text{Ni}_5(\text{TeO}_3)_4\text{Br}_2$ system ($T_N=23$ K and $T_N=30$ K for isostructural Cl and I systems, respectively). In an attempt to shed some more light on the magnetism of $\text{Ni}_5(\text{TeO}_3)_4\text{Cl}_2$, Mihaly *et al.*³ performed a high-field electron magnetic resonance study for frequencies up to 3 THz. Several antiferromagnetic resonance modes were identified and their field-frequency relations were determined. In order to fit the antiferromagnetic resonance data, a collinear spin arrangement was assumed in a magnetic unit cell that is the same as the structural unit cell.³ Since the Ni-centered octahedra are distorted in different ways, one would, however, expect that the Ni^{2+} magnetic moments are not necessary collinear. To investigate the role of the magnetic anisotropy on the magnetic ordering as well as the role of possible frustration imposed by the particular topology of

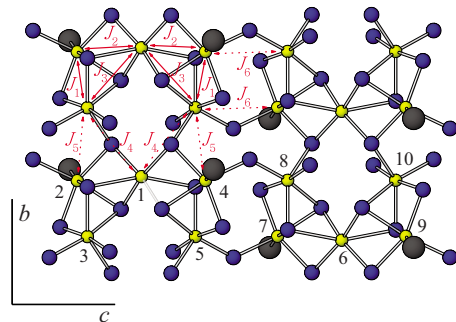


FIG. 1. (Color online) The bc $\text{Ni}_5(\text{TeO}_3)_4\text{Br}_2$ layer and the notation of exchange interactions used in this work. Small yellow circles represent Ni^{2+} moments, larger blue circles stand for oxygen, while gray circles for Br. Te atoms are omitted for clarity. Numbers from 1 to 10 indicate the numbering of magnetic sublattices used in our model.

Ni²⁺ spins, we have preliminary reported on the specific heat, magnetization, and antiferromagnetic resonance measurements in the Ni₅(TeO₃)₄Br₂ single crystal.^{4,5}

In the present paper, we extend our work and report on the detailed analysis of the magnetic properties of Ni₅(TeO₃)₄Br₂ single crystal with magnetization measurements and neutron diffraction and antiferromagnetic resonance data. In a model based on the magnetic unit cell comprising ten Ni²⁺ sublattices, we simultaneously fitted all experiments and thus determined the magnetic structure and the spin Hamiltonian. Magnetic moments associated with the magnetically inequivalent Ni²⁺ sites lie in the a^*c plane, but are far from being collinear. In addition to the Ni-Ni superexchange interactions, a strong single-ion anisotropy is crucial for the understanding of the low-temperature magnetic structure.

II. EXPERIMENTAL DETAILS

A. Sample preparation

The Ni₅(TeO₃)₄Br₂ compound was synthesized by chemical vapor transport reaction. The starting materials were NiO (Alfa Aesar, 99.998%), TeO₂ (Acros, 99.9995%), and NiBr₂ (Alfa Aesar, 99.99%). The large single crystals used in this study were grown from the stoichiometric molar ratios NiO:TeO₂:NiBr₂=4:4:1. The stoichiometric powder was placed in a cleaned fused quartz ampoule and evacuated to a pressure of 10⁻⁵ Torr. In the next step, the HBr (electronic grade) gas was introduced into ampoule at room temperature and finally the tube was sealed. The ampoules were then placed in two zone gradient furnaces. The charge and growth-zone temperatures were 750 and 550 °C, respectively. After four weeks, single crystals of Ni₅(TeO₃)₄Br₂ in the form of orange platelets with a typical size of 10×8×0.2 mm³ grew at the center of the ampoules. The stoichiometry was quantitatively checked by electron-probe microanalysis, and the structure was characterized by x-ray diffraction (XRD).

B. Neutron diffraction experiments

The neutron single crystal experiment has been performed on the TriCS instrument at SINQ, Switzerland, with neutron wavelength of $\lambda=1.18$ Å. A crystal with dimensions 13.6×2.2×0.4 mm³ was mounted in a CCR cooling machine at a four-circle cradle and three data sets at 5, 20, and 35 K have been collected. The longest edge of the crystal corresponds to the b (b^*) direction and the shortest to a^* .

C. Magnetization measurements

Bulk dc magnetic measurements were performed with a Quantum Design superconducting quantum interference device magnetometer in a static magnetic field of 0.1 T in zero-field-cooled and field-cooled runs between room temperature and 2 K. A detailed angular dependence of the magnetization was measured at $T=2$ K in 0.1 T in 5° steps. The measurements were performed along three mutually orthogonal axes a^* , b , and c , previously determined from XRD.

D. Antiferromagnetic resonance measurements

Field-modulated continuous wave high-field magnetic resonance experiments at frequencies ranging from 50 to 550 GHz were performed at the NHMFL facility.⁶ Gunn oscillator⁷ was used as a microwave source in the transmission geometry. Oxford cryogenics cryostat with temperature stability better than ± 0.1 K has been used for low-temperature experiments.

III. MODEL

A. Magnetic structure calculations

Based on the crystal structure, we expect the dominant exchange interactions to take place among Ni²⁺ spins ($S=1$) in the [Ni₅O₁₇X₂] basic building block. The Ni-Ni superexchange pathway includes oxygen bridges, but the exchange coupling between the different Ni sites differs from pair to pair. For instance, the distances between the Ni2 and Ni3 sites and between the Ni1 and Ni2 sites are 2.82 and 2.98 Å, respectively, and their [NiO₆] octahedra connect via face sharing. The distance between the Ni1 and Ni3 is already larger, i.e., 3.29 Å, but the connectivity is now assured by edge sharing. Finally, these building blocks are connected with corner sharing so that the distances between the Ni sites on neighboring [Ni₅O₁₇X₂] units increase to 3.4 Å (Ni3-Ni2), 3.57 Å (Ni3-Ni1), and 3.58 Å (Ni2-Ni3). Other Ni-Ni distances are already larger and the superexchange bridges involve several ligand atoms, making these exchange interactions negligibly small. Also, the exchange interactions between the layers can be neglected too.³

A complete network of Ni sites in a layer projected along the reciprocal a^* direction with the notation of the exchange coupling constants is shown in Fig. 1. Since J_1 and J_5 couplings both act between the Ni2 and Ni3 sites, i.e., former within and latter between the neighboring basic units, only the Ni2-Ni3 effective exchange coupling constant $J'_1=J_1+J_5$ can be determined. The same argument applies also for the J_3 and J_4 exchange couplings between Ni1 and Ni3 sites. The effective exchange constant $J'_3=J_3+J_4$ replaces them in our model.

As mentioned above, the [NiO₆] octahedra are strongly distorted, so we will, in addition to the exchange interaction, assume the presence of significant single-ion anisotropy. We stress that single-ion anisotropy is frequently very relevant for Ni²⁺ ions in distorted [NiO₆] octahedra.⁹⁻¹² Furthermore, there is almost no symmetry restriction for the Dzyaloshinsky-Moriya antisymmetric exchange interaction,¹³ which is thus, in principle, allowed for each Ni pair.

A complete Hamiltonian of our system can therefore be written as

$$\mathcal{H} = \sum_{i>j} \vec{S}_i \cdot \mathbf{J}_{ij} \cdot \vec{S}_j + \sum_j \vec{S}_j \cdot \mathbf{D}_j \cdot \vec{S}_j + \sum_{i>j} \vec{d}_{ij} \cdot (\vec{S}_i \times \vec{S}_j) + \mu_B \sum_j \vec{S}_j \cdot \mathbf{g} \cdot \vec{B}_0. \quad (1)$$

Here, the components of the above Hamiltonian are the ex-

change interaction between nearest neighbors, single-ion anisotropy, Dzyaloshinsky-Moriya antisymmetric exchange interaction, and the Zeeman term. The components of the single-ion anisotropy tensor \mathbf{D}_j depend primarily on the local Ni²⁺ environment and thus are different for the Ni1, Ni2, and Ni3 sites. Applying the molecular field approximation,¹⁴ we can rewrite the above Hamiltonian as a magnetic free energy \mathcal{F} per Ni site,

$$\mathcal{F} = \sum_{i>j} \vec{M}_i \cdot \mathbf{A}_{ij} \cdot \vec{M}_j + \sum_j \vec{M}_j \cdot \mathbf{K}_j \cdot \vec{M}_j + \sum_{i>j} \vec{D}_{ij} \cdot (\vec{M}_i \times \vec{M}_j) - \sum_j \vec{M}_j \cdot \frac{\mathbf{g}}{g} \vec{B}_0. \quad (2)$$

In the above free energy expression, we introduced ten magnetic sublattices (see Fig. 1 for their numbering) with corresponding magnetizations $\vec{M}_j = -Ng\mu_B \langle \vec{S}_j \rangle$, where N is the number of Ni²⁺ magnetic ions in the j th sublattice, g is the g factor of the free electron, and $\langle \cdots \rangle$ indicates the thermal average. The molecular field constants are defined as follows:

$$\mathbf{A}_{ij} = \frac{\mathbf{J}_{ij}}{N(g\mu_B)^2}, \quad (3)$$

$$\mathbf{K}_j = \frac{1}{N(g\mu_B)^2} \mathbf{D}_j, \quad (4)$$

$$\vec{D}_{ij} = \frac{\vec{d}_{ij}}{N(g\mu_B)^2}. \quad (5)$$

In order to calculate the equilibrium orientations of the sublattice magnetizations, we numerically searched for the free energy minimum under the assumption that the magnitudes of the sublattice magnetizations are constants. Once we knew the magnetic structure, we then proceeded with the calculations of the corresponding magnetization curves and susceptibilities. In the final step, we calculated the magnetic resonance modes as follows. We first calculated the effective magnetic field acting on the j th sublattice magnetization,

$$\vec{B}_j = - \frac{\partial \mathcal{F}}{\partial \vec{M}_j}. \quad (6)$$

These effective magnetic fields were then used to write the equations of motion for all sublattice magnetizations,

$$\frac{d\vec{M}_j}{dt} = \gamma \vec{M}_j \times \vec{B}_j, \quad (7)$$

where $\gamma = -g\mu_B/\hbar$ is the gyromagnetic ratio. To make the problem tractable, we assumed harmonic oscillations ($dM_j \propto \exp[i\omega t]$) and linearized equations of motion. The problem can be solved only numerically and the parameters \mathbf{A}_{ij} , \mathbf{K}_j , and \vec{D}_{ij} were adjusted to fit the magnetization curves and frequency as well as the angular dependence of the antiferromagnetic resonance modes.

TABLE I. Calculated components of the single-ion anisotropy tensors \mathbf{D} and the Euler angles α , χ , and γ for their transformations. See text for details.

	Ni1	Ni2	Ni3
D_{zz} (K)	23.83	6.14	-20.58
D_{xx} (K)	-1.72	-1.17	12.41
D_{yy} (K)	-22.11	-4.98	8.17
D (K)	35.75	9.22	-30.87
E (K)	10.20	1.90	2.12
α (deg)	89.99	359.76	309.69
χ (deg)	89.85	56.10	52.66
γ (deg)	270.0	77.47	84.77

B. Calculations of spin parameters

It is obvious from the model described above that we are dealing with a very complicated magnetic structure and that large number of parameters is needed to adequately describe it. For this reason, we decided first to calculate the single-ion anisotropies and then to use these parameters as the input in the fitting procedure.

The orientation of the single-ion anisotropy tensor \mathbf{D} and its principal values were estimated by angular overlap model (AOM) calculations. The method proceeded in two steps. First, the ligand field matrix was constructed and diagonalized with 1000 unique directions of the magnetic field vector. This step was accomplished using program LIGFIELD developed by Bendix.¹⁵ AOM parameters for the Ni-O, Ni-Cl, and Ni-Br bonding interactions were estimated from values of 10Dq documented for homoleptic Ni(II) centers. Values for e_σ and e_π were derived assuming $e_\pi = 0.2e_\sigma$. The parameter e_σ was assumed to vary with distance as a function of $1/r^5$ and e_π as a function of $1/r^6$. The Racah and spin-orbit coupling parameters were fixed at 80% of their free-ion values, and the orbital Zeeman interaction reduced accordingly. Next, the calculated energies of the triplet ground state manifold were modeled by the general $S=1$ spin Hamiltonian $\mathcal{H} = \vec{S} \cdot \mathbf{D} \cdot \vec{S} + \mu_B \sum_j \vec{S}_j \cdot \mathbf{g} \cdot \vec{B}_0$. Least-squares refinement of the eigenvalues of the above Hamiltonian to the three lowest lying eigenvalues of the AOM calculations yielded the \mathbf{D} tensor and \mathbf{g} matrix in the reference coordination frame. The principal values were determined via the transformations $\mathbf{D}' = U_D^{-1} \mathbf{D} U_D$ and $\mathbf{g}' = U_g^{-1} \mathbf{g} U_g$. Here, \mathbf{D}' and \mathbf{g}' refer to the \mathbf{D} tensor and \mathbf{g} matrix in eigencoordinate frames in which they are diagonal. The transformation matrices U_D and U_g contain the direction cosines relating the two coordinate systems, from which the Euler angles can be calculated. The results of the calculations are summarized in Table I. Here, we also introduced the standard planar anisotropy $E = \frac{1}{2}(D_{xx} - D_{yy})$ and $D = D_{zz} - \frac{1}{2}(D_{xx} + D_{yy})$ axial anisotropy constants.

It is important to emphasize the extent to which the single-ion anisotropy can be estimated from these AOM calculations. The ratio $E:D$ is governed principally by the angular disposition of the ligands, obtained from the crystallographic data, and the relative strength of the bonding interactions. We are therefore confident that our estimates of

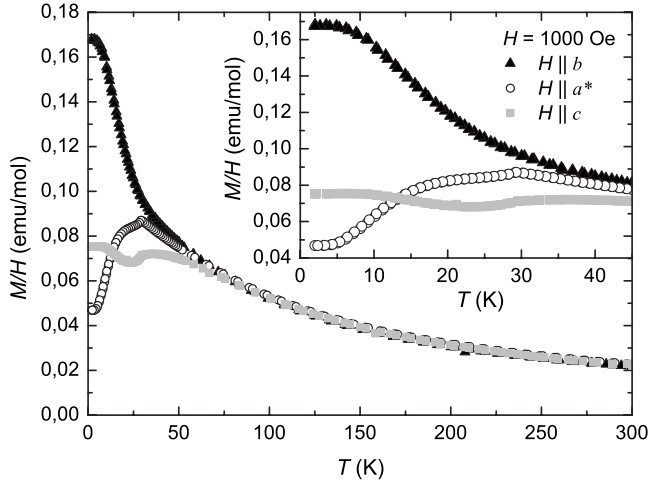


FIG. 2. The temperature dependence of dc magnetic susceptibility measured for different crystal orientations. In the inset, we show the expanded low-temperature region.

the bonding interactions are reasonable and hence the ratio of E to D should be quite reliable. We have allowed for covalency by reducing the Racah and spin-orbit coupling parameters to 80% of their free-ion values. However, the reduction of these parameters could conceivably be somewhat different with the result that the absolute magnitude of the splitting of the 3^A term is likely to differ from the values computed. Finally, the reader will note that the calculated anisotropy of the Ni1 center is very large with D_{zz} and D_{yy} of similar magnitude. In this instance, it is difficult to establish with certainty the orientation of the \mathbf{D} tensor by the least-squares fitting procedure adopted.

IV. RESULTS

A. Magnetization measurements

Temperature dependence of the dc magnetic susceptibility measured in a field of 1 kOe is for different crystal orientations shown in Fig. 2. At high temperatures, the magnetic susceptibility follows the Curie-Weiss law with the Curie-Weiss temperature of about $\theta_C \sim -50$ K and the Curie constant $C = 75-80$ A m² K/mol T as expected for an $S=1$ spin system. A complete analysis of the high-temperature susceptibility data can be found in Ref. 5. The sign and the magnitude of the Curie-Weiss temperature suggest fairly strong predominantly antiferromagnetic interactions between Ni²⁺ moments. There is a small magnetic anisotropy present already at high temperatures, which we attribute to the anisotropy in the g factor.

A closer inspection of the low-temperature susceptibility data (inset of Fig. 2) reveals a small bump at $T_N = 29(1)$ K reported already in the original article and attributed to the antiferromagnetic transition. Below T_N , a large anisotropy in the magnetic response was found. Since the largest magnetization is measured along the $b \parallel H$ axis, we assign this axis as the crystalline effective intermediate axis. This also means that the crystalline a^*c plane is the plane of the easy and the

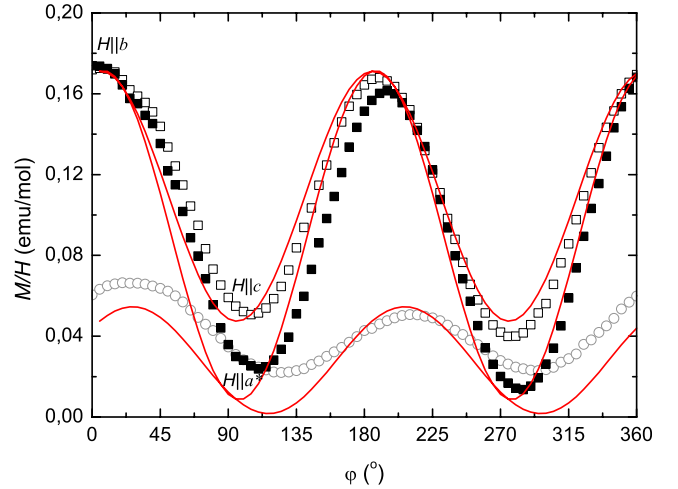


FIG. 3. (Color online) The angular dependence of the magnetization measured at $T=2$ K for crystal rotations in the a^*c , a^*b , and bc planes. Solid lines are fits to the model described in the text.

hard axes. Comparing the measurements taken with $a^* \parallel H$ and $c \parallel H$, we notice that the decrease of the magnetic susceptibility is larger for $a^* \parallel H$. We therefore conclude that this crystal axis is close to an effective crystalline easy axis which leaves us with $c \parallel H$ as the effective hard axis. The complete temperature dependence of the magnetic susceptibility, however, signals even more complex picture of the magnetism in Ni₅(TeO₃)₄Br₂ single crystal. For instance, we notice a bump in the magnetic susceptibility at around $T = 12$ K, which could, for instance, originate from the different temperature dependence of the Ni sublattice magnetizations.

To determine the precise orientation of the magnetization easy and hard axes, we decided to measure the angular dependence of the magnetization (Fig. 3) at $T=2$ K and $H = 1000$ Oe. The magnetization is the largest for $b \parallel H$ confirming once again this axis as the intermediate axis (see above discussion for the argumentation). In the crystalline a^*c plane, the easy axis is tilted $\sim 30^\circ$ from the crystal a^* axis, while the hard axis is then $\sim 30^\circ$ from the c axis.

B. Neutron diffraction measurements

We now turn to the determination of the magnetic structure by neutron diffraction. A refinement of the crystal structure for Ni₅(TeO₃)₄Br₂ single crystal confirmed the structural model published in Ref. 2. Below T_N , new reflections of magnetic origin appeared at the positions of the C-centered lattice corresponding to the wave vector $\mathbf{k}=(0,0,0)$ (see Table II). The two strongest magnetic peaks (-201) and (-203) break the extinction rule $h0l: h, l=2n$, while the $hk0: h+k=2n$ rule is preserved.

To facilitate magnetic structure determination, representation analysis was performed with the program BASIREPS.⁸ The Fourier coefficients describing possible spin configurations can be written as linear combinations of irreducible representations of the wave vector group. The group of $\mathbf{k}=(0,0,0)$ does not split the $4e$ and $8f$ Wyckoff sites occupied

TABLE II. Selected observed and calculated squared magnetic structure factors F_{obs}^2 and F_{calc}^2 of $\text{Ni}_5(\text{TeO}_3)_4\text{Br}_2$ single crystal at 5 K corresponding to the model discussed in the text. The data set of 90 reflections with $h_{max}=12$, $k=0$, and $l_{max}=13$ was used to refine the magnetic structure.

h	k	l	F_{obs}^2	F_{calc}^2
0	0	1	0.09	0.15
0	0	3	14.51	12.95
0	0	5	2.82	3.79
0	0	7	3.07	0.64
0	0	9	0.73	0.01
0	0	11	0.84	2.19
0	0	13	0.94	0.28
0	0	15	0.99	0.01
2	0	-1	30.43	29.49
2	0	-3	65.56	71.14
2	0	-5	0.96	1.86
-2	0	7	4.10	0.52
2	0	-9	1.54	0.00
2	0	-11	3.93	3.04
2	0	-13	0.90	0.78
2	0	1	1.51	0.01
2	0	3	2.36	3.10
2	0	5	3.27	2.89
2	0	7	1.68	0.24
2	0	9	2.36	0.04
2	0	11	2.25	0.79
2	0	13	2.90	0.21
4	0	1	0.35	0.06
4	0	3	4.39	3.04
4	0	5	2.13	0.36
4	0	7	0.86	0.43
4	0	9	1.09	0.05
4	0	11	1.00	0.26
4	0	-1	12.00	11.77
4	0	-3	60.73	59.33
4	0	-5	11.51	7.26
4	0	-7	1.23	1.86
4	0	-9	3.08	2.37
4	0	-11	1.23	2.07
4	0	-13	1.51	1.98

by Ni^{2+} ions. The magnetic representations for the $4e$ and $8f$ sites are

$$\Gamma(4e) = 1\Gamma_1 + 1\Gamma_2 + 2\Gamma_3 + 2\Gamma_4,$$

$$\Gamma(8f) = 3\Gamma_1 + 3\Gamma_2 + 3\Gamma_3 + 3\Gamma_4.$$

The best agreement with experimental data was obtained for the irreducible representation Γ_4 (see Table III) corresponding to the $C2'/c$ magnetic group. The moments of Ni^{2+} ions of the same Wyckoff site related by the inversion center i' or

TABLE III. Irreducible representation Γ_4 of the wave vector group for $\mathbf{k}=(0,0,0)$ in the space group $C2'/c$. The coefficients corresponding to the Wyckoff sites $4e$ are $x=0.5$, $y=0.2575$, $z=0.25$ for Ni1 and those of $8f$ are $x=0.4089$, $y=0.2842$, $z=0.0265$ for Ni2 and $x=0.5095$, $y=0.7191$, $z=0.1213$ for Ni3.

$4e$					
x	y	z	u	v	w
$-x+1/2$	$-y+1/2$	$-z+1/2$	$-u$	0	$-v$
$8f$					
x	y	z	u	v	w
$-x+1$	y	$-z+1/2$	u	$-v$	w
$-x+1/2$	$-y+1/2$	$-z+1/2$	$-u$	$-v$	$-w$
x	$-y+1$	$z+1/2$	$-u$	v	$-w$

by the glide plane c are oppositely aligned. The two-dimensional canted magnetic structure is presented in Fig. 4, the agreement between observed and calculated integrated magnetic reflection intensities is given in Table II, and the refined values for Ni^{2+} moments are summarized in Table IV. We first note that the Ni^{2+} magnetic moments are confined in the ac plane with the major component along the $[101]$ diagonal, reaching the values $2.16(9) \mu_B/\text{Ni}1$, $2.15(5) \mu_B/\text{Ni}2$, and $2.19(6) \mu_B/\text{Ni}3$ at 5 K. It is also clear from the refined magnetic structure that the Ni^{2+} moments are far from being collinear and the tilt from the c axis varies from site to site. There is, however, a tendency of the nearest Ni2 and Ni3 moments to align in the same direction and “opposite” to the Ni1 moment.

The temperature evolution of the magnetic arrangement can be extracted from the temperature dependence of the (-201) and (-203) reflections and from the refinement of single crystal data collected at 5 and 20 K. Figure 5 shows that the (-201) and (-203) reflections have very different although correlated temperature dependence. When increasing temperature from 5 to 15 K, the intensity of the (-201) reflection, in contrast to the (-203) reflection, first slightly increases and for $T > 15$ K becomes stronger. Above 15 K, (-201) stays almost constant up to ~ 24 K and then dramatically reduces approaching T_N from below. Such behavior correlates well with the temperature dependence of the magnetization measured for $H \parallel c$ (Fig. 2). On the other hand, the

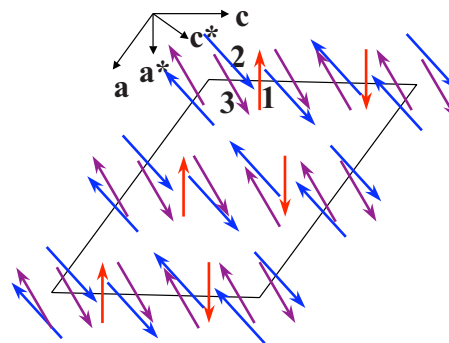


FIG. 4. (Color online) The ac projection of the unit cell of the magnetic structure of $\text{Ni}_5(\text{TeO}_3)_4\text{Br}_2$.

TABLE IV. Refined parameters for the neutron data $\text{Ni}_5(\text{TeO}_3)_4\text{Br}_2$ in magnetically ordered state at $T=5$ K and $T=20$ K. μ_B is the ordered magnetic moment and θ the tilt from the c^* axis.

T (K)	Ni^{2+}	μ_B	θ (deg)
5	1	2.16(9)	241(2)
	2	2.15(5)	20(2)
	3	2.19(6)	32(2)
$R_M=13.1\%$			
20 K	1	1.5(1)	242(4)
	2	1.90(7)	14(3)
	3	1.97(8)	23(3)
$R_M=18.8\%$			

temperature dependence of the (-203) intensity is much less dramatic and decreases with increasing temperatures as $A(1 - T/T_N)^{2\beta}$ with $\beta=0.25(1)$. Although deeper understanding of the critical exponent β has to await for the detailed theoretical work, we note that $\beta=0.25$ is typical for the stacked-triangular antiferromagnets.¹⁶ The observed temperature dependence of the intensities of the magnetic reflections can have two origins: either a gradual rotation of the moments or the nonuniform temperature dependence of the magnetic moment values of different Ni sites. Closer inspection of the magnetic structure factors of these two reflections shows that several factors determine such different temperature dependence. Firstly, due to the special position \mathbf{r} occupied by the Ni1 ions, the $\sin(2\pi\mathbf{h}\mathbf{r})$ contribution of this site adds up to the contributions of the other Ni sites for $\mathbf{h}=(-201)$ and is subtracted for (-203) . Secondly, as presented in the inset of Fig. 5, the (-201) reciprocal lattice direction is almost par-

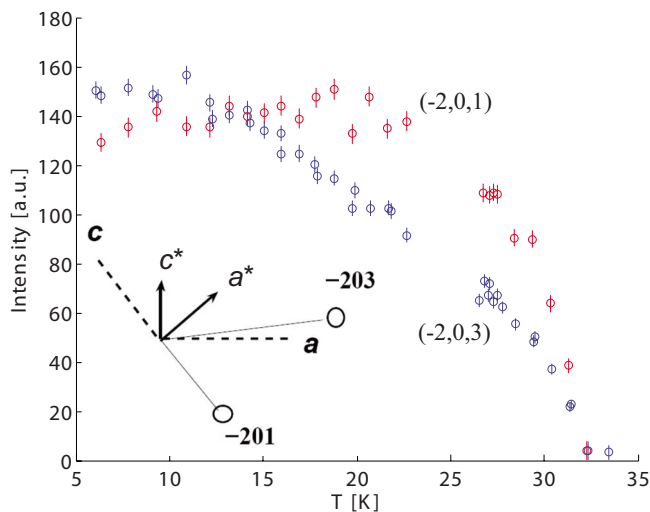


FIG. 5. (Color online) Measured intensity of the (-201) and (-203) magnetic reflections of $\text{Ni}_5(\text{TeO}_3)_4\text{Br}_2$ single crystal as a function of temperature. Inset: The (-201) reciprocal lattice direction is almost parallel to c , while the (-203) direction is almost parallel to the a axis.

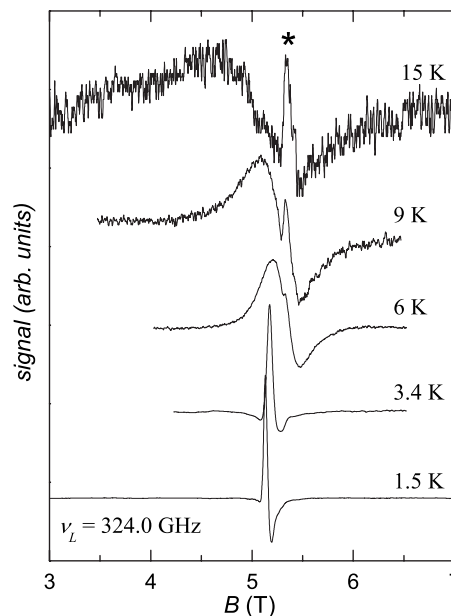


FIG. 6. The temperature dependence of the antiferromagnetic resonance line shape measured at a Larmor frequency $\nu = 324$ GHz. A narrow spike at $B_r=5.3$ T and marked with asterisk is due to the oxygen resonance.

allel to the c axis, while the (-203) direction is almost parallel to the a axis. Due to the dipole interaction between the neutron and the magnetic moments, only components perpendicular to the scattering vector contribute to scattered intensity. Therefore, the (-201) reflection is sensitive to the M_x component and (-203) to M_z . Finally, as the magnetic moment of Ni1 is oppositely aligned to the Ni2 and Ni3 moments, the decrease of the Ni1 moment would increase the (-201) magnetic intensity and decrease the (-203) one. Comparison of the magnetic arrangements refined at 20 and 5 K in the $\text{Ni}_5(\text{TeO}_3)_4\text{Br}_2$ single crystal confirms that the temperature dependence of the Ni1 moment is different from those of Ni2 and Ni3. It decreases faster [by 67(5)%] than the other two moment values [87(4)% for Ni2 and 92(4)% for Ni3], leading to different temperature dependences of the (-201) and (-203) reflections.

C. Antiferromagnetic resonance

1. Temperature dependence

Our attempts to detect electron paramagnetic resonance already in the paramagnetic phase, i.e., for $T > 29$ K, were not successful. We tried in a broad frequency range for resonance frequencies between 9.7 and 330 GHz. Apparently, the resonance is so broad that it is currently beyond the detection limit of our experimental equipment. On the other hand, we were able to detect the resonance in the antiferromagnetic phase (Fig. 6) but only for temperatures below $T \sim 15$ K, i.e., deep in the antiferromagnetic phase. The resonance signal measured at $\nu_L=324$ GHz and for the crystal orientation $a^* \parallel H$ is, at $T=15$ K, very broad as the peak-to-peak line-width is 1.8 T. The resonance is also shifted toward lower

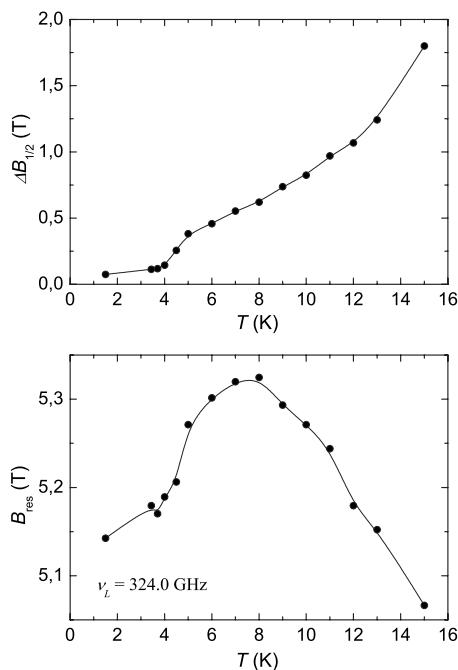


FIG. 7. The temperature dependence of the (a) the linewidth and (b) the center of the antiferromagnetic resonance mode.

fields (resonance field is at 5.05 T) compared to the position expected for a usual Ni^{2+} $g \sim 2.5$ paramagnetic signal (11.45 T). The extra spike marked with asterisk in Fig. 6 is due to the oxygen resonance and will be thus from now on ignored. The main resonance has nearly Lorentzian line shape (the spectra shown in Fig. 6 are distorted due to the admixture of dispersion into our signal).

On cooling to low temperatures, the signal changes very dramatically. The first immediate observation is that the signal gets significantly narrower with decreasing temperature. A temperature dependence of the linewidth is shown in Fig. 7(a). The linewidth decreases from $\Delta B_{1/2} = 1.8(1)$ T at $T = 15$ K to $\Delta B_{1/2} = 0.07(1)$ T at $T = 1.5$ K. Above $T = 15$ K, the linewidth shows nearly divergent dependence, and for this reason, we were not able to detect signal above this temperature. We also notice a small change in the slope in the temperature dependence of the linewidth at around $T = 5$ K. The temperature dependence of the center of the resonance is also very complex [Fig. 7(b)]. The resonance field first increases with decreasing temperature, reaching a maximum at $T = 8$ K. Below this temperature, the trend reverses and the center of the line now shifts toward lower fields with decreasing temperature. Such temperature dependence of the center of the line could signal a very complex temperature dependence of individual Ni^{2+} moments as already inferred from the neutron diffraction data.

2. Frequency dependence

In this section, we now turn to the frequency dependence of the resonance signal described above. A full frequency dependence was measured at $T = 4$ K, i.e., well below T_N . A very typical observation for the resonance mode shown in

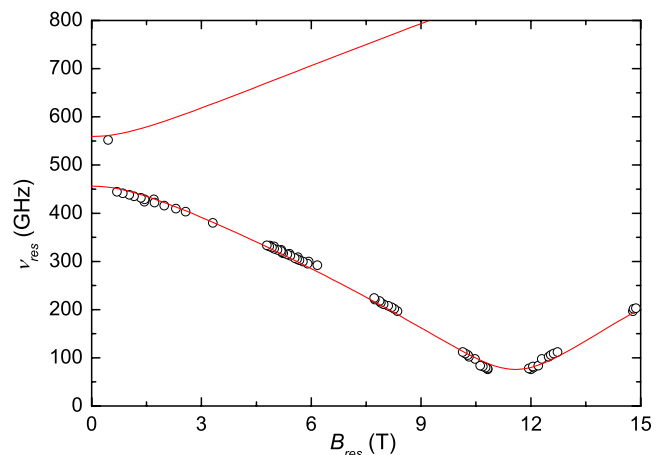


FIG. 8. (Color online) The frequency dependence of the two lowest antiferromagnetic resonance modes (open circles). The solid line represents a fit to a model described in the text.

Fig. 6 is that the center of the resonance shifts to higher resonance fields with decreasing resonance frequency.⁴ A full dependence of resonance-frequency–resonance-field relation for crystal orientation $a^* \parallel B$ is shown in Fig. 8. We note that such behavior is very typical for the antiferromagnetic resonance modes. In fact, in a very recent publication, Mihaly *et al.*³ found ten resonance modes in a frequency range up to 3 THz in $\text{Ni}_5(\text{TeO}_3)_4\text{Cl}_2$ system. Our mode corresponds to their lowest resonance mode. This particular mode softens with increasing field until $B = B_{sf}$. At spin-flop field, the resonance field goes toward zero, and for $B > B_{sf}$, resonance frequency increases with resonance field again. From the present data, one can determine the spin-flop field to be ~ 10.7 T. We also stress that we managed to detect the next higher resonance mode. At zero field, the two modes split into two branches, i.e., the zero-field frequency is for the lowest mode $\omega_1(0) = 450(5)$ GHz, while it is for the second mode $\omega_1(0) = 550(8)$ GHz. The zero-field frequencies and the splitting of the two lowest modes confirm the importance of magnetic anisotropies in our system. The zero-field resonance frequency is for a simple two-sublattice model given by $\omega(0) = \gamma \sqrt{B_A(B_A + 2B_E)}$, where B_A and B_E are magnetic anisotropy and exchange field respectively. As pointed out already by Mihaly *et al.*,³ the zero-field degeneracy of the modes can be removed by the presence of Dzyaloshinsky-Moriya interaction and the two modes should then vary as $\omega = \omega(0) \pm \gamma \sqrt{B^2 + B_{DM}^2}$, where B_{DM} is the field related to the strength of the Dzyaloshinsky-Moriya interaction. On the other hand, the same effect can be achieved by the presence of nonaxial anisotropy field. In fact, our calculations and magnetization studies presented above strongly suggest that this term could be large and therefore needs to be taken into account.

3. Angular dependence

In the next step, we have measured the angular dependence of the lowest resonance modes. The variation of the resonance field with the angle of rotation is shown in Fig. 9.

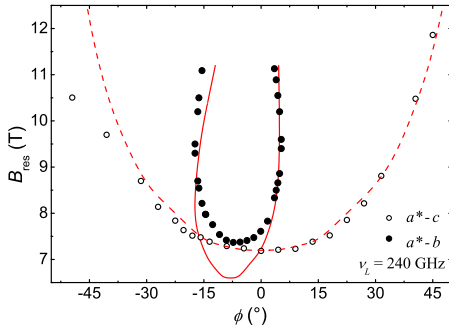


FIG. 9. (Color online) The angular dependence of the antiferromagnetic resonance mode in the a^*b plane (solid circles) as well as in the a^*c plane (open circles). The Larmor frequency was set to $\omega_L=240$ GHz and the temperature was $T=4$ K. Solid lines are fits to a model described in the text.

A very strong variation of the resonance field with the angle is seen in the a^*b plane. Analogous but less dramatic dependence is seen for the rotations in the a^*c plane. This observation holds for both resonances on each side of the dip in the resonance-field–resonance-frequency relation. The angular dependence is so strong that we were able to follow the resonance modes only up to 15° away from the a^* in the a^*b plane. In this plane, for angles larger than that angle, the resonance mode is already higher than the experimental Larmor frequency $\omega_L=240$ GHz and thus becomes unobservable.

V. DISCUSSION

Let us now make a brief summary of main experimental findings.

(1) $\text{Ni}_5(\text{TeO}_3)_4\text{Br}_2$ unambiguously undergoes a transition to an antiferromagnetically ordered state below the Néel temperature $T_N=29$ K.

(2) In the antiferromagnetic phase, Ni^{2+} magnetic moments are ordered in the a^*c plane. The magnetization measurements identify the a^* axis as being close to the effective easy axis, while the c axis as close to the hard axis (more precisely, the two magnetization axes are tilted by 30° away from the crystallographic axes). The b axis is the intermediate axis.

(3) The magnetic unit cell is equal to the crystallographic one and it is made of two $[\text{Ni}_5\text{O}_{17}\text{Br}_2]$ units with a zero total magnetic moment. The two Ni^{2+} magnetic moments, Ni2 and

Ni3, are nearly parallel, while the central Ni1 moment is significantly canted away from their principal direction.

(4) Nonmonotonic temperature dependence of the magnetization as well as the intensity of (-201) and (-203) magnetic reflections below T_N suggest that Ni1 and Ni2,3 magnetic moments have different temperature dependences.

(5) In our high-field magnetic resonance experiments, we were able to detect the two lowest antiferromagnetic resonance modes with the zero-field gap for the lowest mode at 450 GHz. A very pronounced angular dependence of the resonance modes is rather typical of antiferromagnetic resonance.

(6) The spin-flop field was determined to be $B_{sf}=10.7$ T at $T=4$ K judging from the softening of the lowest antiferromagnetic resonance mode. These findings underline the importance of magnetic anisotropy for the magnetic ground state of $\text{Ni}_5(\text{TeO}_3)_4\text{Br}_2$.

We are now in the position to apply the model described in Sec. III. Since the number of parameters in the magnetic free energy [Eq. (2)] is large, we need to make certain assumptions to make the problem tractable. As mentioned above, in the basic unit, the Ni2 and Ni3 moments are nearly collinear (Fig. 4), so we will assume the ferromagnetic J'_1 interaction between these two spins. On the other hand, the Ni1 moment tends to point in the opposite direction (although tilted away from the direction defined by Ni2 and Ni3 moments). For this reason, we assume that the exchange interactions between Ni2 and Ni1 (J_2), as well as between Ni3 and Ni1 (J'_3), are antiferromagnetic. From the orientation of the spins in the two $[\text{Ni}_5\text{O}_{17}\text{Br}_2]$ units forming the magnetic unit cell (Fig. 1), we anticipate the antiferromagnetic interactions J_6 . To account for tilting of the Ni moments in the a^*c plane, we use the calculated site dependent single-ion anisotropies (Table I) but left the scaling of the eigenvalues as a free parameter. The simulation strategy was to model the free energy [Eq. (2)] in order to describe simultaneously the magnetic structure (i.e., the equilibrium orientations) obtained from the neutron diffraction (Fig. 4), the angular dependence of the magnetization (Fig. 3), and the frequency (Fig. 8) and angular (Fig. 9) dependence of the antiferromagnetic resonance data. The final set of parameters consistent with all experiments is given in Table V. In order to obtain the magnetic structure (Fig. 4), we also added the Dzyaloshinsky-Moriya exchange interactions between the Ni1 and Ni2 sites [$\vec{d}_{1,2}=(0, -5.2 \text{ K}, 0)$] and between the Ni2 and Ni3 sites [$\vec{d}_{2,3}=(0, 0.1 \text{ K}, 0)$]. The fact that we were able to simultaneously describe three different experiments sug-

TABLE V. Summary of parameters used for fitting of the neutron diffraction, magnetization, and antiferromagnetic resonance data measured on $\text{Ni}_5(\text{TeO}_3)_4\text{Br}_2$ single crystal. The orientations of single-ion anisotropy tensors \mathbf{D}_i are the same as in Table I.

	\mathbf{J}_1 (K)	\mathbf{J}_2 (K)	\mathbf{J}_3 (K)	\mathbf{J}_6 (K)	\mathbf{D}_1 (K)	\mathbf{D}_2 (K)	\mathbf{D}_3 (K)
x	-0.8	34.7	56.4	10.7	-0.8	-0.6	6.1
y	-19.6	18.4	49.6	2.0	-10.8	-2.4	4.0
z	-1.2	5.8	12.6	25.4	11.6	3.0	-10.0

gests that our parameters are close to the correct values.

The empirical measure of frustration¹⁷ is given by the ratio between the Curie-Weiss temperature $\theta_C = -50$ K and the Néel temperature $T_N = 29$ K, which is in our case $f = |\theta_C|/T_N = 1.7$. Since materials with f larger than 10 are considered as strongly frustrated materials, we conclude that the frustration effects implied by the Ni^{2+} topology are not very pronounced in the $\text{Ni}_5(\text{TeO}_3)_4\text{Br}_2$ system. The effective ferromagnetic interaction between Ni2 and Ni3 seems to explain that. The remaining frustration is, in fact, a consequence of the large magnetic anisotropies. The spin Hamiltonian parameters show that the single-ion anisotropy of Ni^{2+} is significant and is of the same order of magnitude as the exchange interactions. We notice, however, a peculiarity of the Ni3 site, which has a different sign for D (see Tables I and V). It may well be that the Ni3 site anisotropy is responsible for the peculiar temperature dependence of the Ni moments detected by neutron diffraction as well as by the magnetization experiments. The large single-ion anisotropy constants originate from the strongly distorted Ni^{2+} octahedral surroundings. The difference in the single-ion anisotropy direction implied by the different directions of the octahedral deformations is the main reason for the Ni^{2+} moment tilting and for the noncollinear low-temperature magnetic structure. At the same time, the magnetic anisotropy further suppresses quantum fluctuations arising from the geometrical frustration and stabilizes the long-range antiferromagnetic ordering below T_N . It is therefore clear that the single-ion anisotropy in

addition to exchange anisotropy plays a vital role in $\text{Ni}_5(\text{TeO}_3)_4\text{Br}_2$ system. Our results thus contradict the model proposed for isostructural $\text{Ni}_5(\text{TeO}_3)_4\text{Cl}_2$ by Mihaly *et al.*,³ where the single-ion anisotropy was neglected.

VI. CONCLUSIONS

In conclusion, the magnetic properties of $\text{Ni}_5(\text{TeO}_3)_4\text{Br}_2$ single crystal were investigated by magnetization, neutron diffraction, and antiferromagnetic resonance measurements. The antiferromagnetic ground state found below $T_N = 29$ K is described by a noncollinear Ni^{2+} ($S=1$) order. Theoretical analysis of the data with the molecular field formalism emphasized the presence of the strong single-ion anisotropies in addition to the exchange anisotropy. These anisotropies prevail over the geometrical frustration and lead to a long-range magnetic ordering with the noncollinear sublattice structure.

ACKNOWLEDGMENTS

D.A. acknowledges fruitful discussions with Janez Bonča, Faculty of Mathematics and Physics, University of Ljubljana, Slovenia. The neutron diffraction work was performed at SINQ, Paul Scherrer Institute, Villigen, Switzerland. This work was supported by the Swiss National Science Foundation through the MaNEP NCCR. We would like to thank F. Bussy (University of Lausanne) for the microprobe analysis.

*oksana.zaharko@psi.ch

†denis.arcon@ijs.si

¹A. P. Ramirez, *Annu. Rev. Mater. Sci.* **24**, 453 (1994).

²M. Johansson, K. W. Tornroos, P. Lemmens, and P. Millet, *Chem. Mater.* **15**, 68 (2003).

³L. Mihaly, T. Feher, B. Dora, B. Nafradi, H. Berger, and L. Forro, *Phys. Rev. B* **74**, 174403 (2006).

⁴D. Arčon, A. Zorko, J. Dolinšek, H. Berger, A. Ozarowski, H. van Tol, and L. C. Brunel, *J. Magn. Magn. Mater.* **316**, E349 (2007).

⁵A. Zorko, D. Arčon, J. Dolinšek, Z. Jagličič, A. Jeromen, H. van Tol, L. C. Brunel, and H. Berger, *J. Phys.: Condens. Matter* **19**, 145278 (2006).

⁶A. K. Hassan, L. A. Pardi, J. Krzystek, A. Sienkiewicz, P. Goy, M. Rohrer, and L. C. Brunel, *J. Magn. Reson.* **142**, 300 (2000).

⁷J. van Tol, L. C. Brunel, and R. J. Wylde, *Rev. Sci. Instrum.* **76**, 074101 (2005).

⁸J. Rodriguez-Carvajal, *Physica B* **192**, 55 (1993).

⁹D. Alders, R. Coehoorn, and W. J. M. de Jonge, *Phys. Rev. B* **63**, 054407 (2001).

¹⁰V. Kataev, C. Golze, A. Alfonsov, R. Klingeler, B. Buechner, M. Goiran, J. M. Broto, H. Rakoto, C. Mennerich, H. H. Klaus, S. Demeshko, G. Leibel, and F. Meyer, *J. Phys.: Conf. Ser.* **51**, 351 (2006).

¹¹A. Orendáčova, M. Orendáč, Z. Travniček, and M. W. Meisel, *Phys. Status Solidi A* **196**, 278 (2003).

¹²R. Becker, M. Prester, H. Berger, M. Johansson, D. Drobac, and I. Zivkovic, *Solid State Sci.* **9**, 223 (2007).

¹³A. Bencini and D. Gatteschi, *EPR of Exchange Coupled Systems* (Springer-Verlag, Berlin, 1990).

¹⁴H. Rohrer and H. Thomas, *J. Appl. Phys.* **40**, 1025 (1969).

¹⁵J. Bendix, LIGFIELD, Department of Chemistry, University of Copenhagen, Denmark.

¹⁶See, for instance, H. Kawamura, *J. Phys.: Condens. Matter* **10**, 4707 (1998).

¹⁷A. P. Ramirez, *J. Appl. Phys.* **70**, 5952 (1991).